









Cite this: *Analyst*, 2019, **144**, 4362

Fluorescence imaging of stained red blood cells with simultaneous resonance Raman photostability analysis†

Ansam J. Talib, ^{a,b} Andrew Fisher, ^e Dmitri V. Voronine, ^{*c,d}
Alexander M. Sinyukov, ^a Sandra C. Bustamante Lopez,^{a,e} Sharad Ambardar, ^{c,d}
Kenith E. Meissner, ^e Marlan O. Scully^{a,f} and Alexei V. Sokolov ^{a,f}

Optical spectroscopic imaging of biological systems has important applications in medical diagnosis, biochemistry, and image-guided surgery. Vibrational spectroscopy, such as Raman scattering, provides high chemical selectivity but is limited by weak signals and a large fluorescence background. Fluorescence imaging is often used by introducing specific dyes in biological systems to label different system parts and to increase the image contrast. However, the extrinsic fluorescence of the staining molecules often masks the intrinsic vibrational signals of biomolecules, which could also be simultaneously detected using the same excitation laser source. Therefore, fluorescence staining is often accompanied by the loss of other important complimentary information. For example, the high laser power often used for the rapid, high-quality imaging could lead to photo-induced suppression or bleaching of the fluorescence and Raman signals resulting in sample photodamage. Therefore, simultaneous imaging and photodamage analysis need to be performed in a controlled bioimaging experiment. Here we perform simultaneous spectroscopic bioimaging and photostability analysis of rhodamine 6G (R6G) stained red blood cells (RBCs) using both fluorescence and resonance Raman imaging in a single 532 nm laser excitation experiment. We develop a corresponding data processing algorithm which allows separation of the two spectroscopic signals. We control the relative intensity of the R6G and RBC signals by varying the excitation laser power and simultaneously monitor the photostability of RBCs. We observe no significant photodamage of RBCs through the absence of changes in the relative Raman peak intensities. Conversely, the R6G molecules show bleaching with the suppression of both the fluorescence and resonance Raman signals. Our approach may be generalized to other types of stained cells with the appropriate selection of fluorescent dyes and excitation sources.

Received 26th April 2019,
Accepted 5th June 2019

DOI: 10.1039/c9an00757a

rsc.li/analyst

1 Introduction

Biomedical optical imaging has been revolutionized by recent developments in light sources and spectroscopic techniques.^{1–3} For example, fluorescence and Raman spectroscopies have been widely used in imaging a variety of biological systems including single biomolecules, cells, tissues, and

whole organisms.^{4–6} Different spectroscopic techniques have advantages and disadvantages which are often complementary and can be used selectively or combined to address specific problems. Fluorescence signals are typically orders of magnitude stronger than Raman signals. However, biological systems often lack chemically-specific fluorescence signals in the visible spectral range and require fluorescent dye staining to improve the imaging contrast. Staining complicates the experimental preparation process and may influence biological functions.⁷ On the other hand, Raman spectroscopy is label-free, allowing study of the sample in its native state. Weak Raman signals may be enhanced using methods such as surface enhancement, coherence, or electronic resonance effects. Both fluorescence and Raman imaging benefit from high intensity lasers, which can lead to laser-induced sample damage and disruption of biological functions. High laser powers are especially useful for super-resolution imaging when the signals originate from nanoscopic sample volumes

^aInstitute for Quantum Science and Engineering, Texas A&M University, College Station, TX 77843, USA

^bDepartment of Physics, University of Thi-Qar, Thi-Qar, Iraq

^cDepartment of Physics, University of South Florida, Tampa, FL 33620, USA.

E-mail: dmitri.voronine@gmail.com

^dDepartment of Medical Engineering, University of South Florida, Tampa, FL 33620, USA

^eDepartment of Physics, Centre for Nanohealth, Swansea University, Swansea, SA2 8PP Wales, UK

^fDepartment of Physics, Baylor University, Waco, TX 76706, USA

† Electronic supplementary information (ESI) available. See DOI: 10.1039/c9an00757a

with few or single molecules of interest.^{8,9} In order to perform bioimaging using these techniques, the effects of the laser intensity on the photostability of biomolecules and live cells must be precisely determined. The challenges of rapid nondestructive spectroscopic imaging in biological media require developing new approaches for simultaneous bioimaging and estimation of the cell stability due to possible photodamage.

Here, we perform optical imaging of one of simple stained cells, *i.e.* rhodamine 6G stained red blood cells (R6G-stained RBCs), using a combination of fluorescence and resonance Raman scattering. R6G is a typical fluorescent dye used as the lasing gain media and for the staining of biological systems.^{10,11} It is also a common Raman reporter molecule used for improving the Raman imaging contrast and as a Raman marker in biosensing.^{12–15} R6G was specifically chosen because its fluorescence and resonance Raman signals are both relatively strong and may be obtained using 532 nm laser excitation. Fluorescence of R6G has also been used in super-resolution optical imaging.¹⁶ We selected a simple biological cell, RBC, whose main constituent protein component, hemoglobin (Hb), provides a strong resonance Raman signal upon 532 nm laser excitation which coincides with the fluorescence and resonance Raman signals of R6G. By staining the RBC with R6G, we designed a stained biological model system which can be used for multi-component bioimaging within a single experimental setup using a single excitation source. This approach allows simultaneous exploration of several effects including fluorescence and resonance Raman bleaching of the stain, and photostability of the biological system. RBCs are critical for the transport of oxygen to the cells in the body. They provide an ideal platform to study oxygenation capability using resonance Raman spectroscopy.^{17–20} Laser-induced photodamage in RBCs has also been probed using Raman spectroscopy.²¹ Various excitation sources with wavelengths from the near-UV to near IR were previously used. Our 532 nm excitation matches the electronic resonance transitions in both R6G and Hb, and therefore, provides the optimal resonance enhancement of the Raman signals of both R6G and RBC. This is accompanied by the simultaneous bleaching of the fluorescence of R6G, which can be precisely controlled and monitored by tuning the laser intensity. Using this control parameter, we detected Hb Raman signals in the presence of the strong R6G fluorescence, and R6G Raman signals in the presence of a strong Hb Raman contribution. Since R6G forms a monolayer on the surface of RBCs, its Raman signal is weak compared to Hb. However, R6G has a larger absorption coefficient and larger bleaching decay rates than Hb.²² The bleaching of both fluorescence and resonance Raman signals of R6G are achieved before any noticeable changes in the Raman spectra of Hb occur. The competition between these resonant signals allows the detection of R6G and Hb in the RBCs under various conditions while probing the photostability of stained RBCs. These results provide a step towards improving real-time multicomponent cellular imaging with high resolution and simultaneous photostability control.

2 Materials and methods

Bovine blood was provided by the Veterinary Medical Park, TAMU. 5 ml of the bovine blood was placed into a 15 ml tube and was centrifuged at 9000 rpm for 5 min. The supernatant and buffy coat were discarded and RBCs were re-suspended in 10 ml of phosphate-buffered saline (PBS). Again, RBCs were centrifuged (9000 rpm for 3 min) and the supernatant was discarded. The preparation of R6G-stained RBCs was performed by mixing the solutions of RBCs with the 10^{-3} M R6G. During this process, R6G adsorbs on the RBC membrane to form stained cells having both Hb and R6G components. Finally, R6G-stained RBCs were either air dried on a glass substrate and were used for imaging immediately (referred to as dried fresh cells), or were air dried after 1-week of storage and used for imaging (referred to as 1-week old cells). The 1-week old cells were used to investigate the effects of the laser power dependence on the photodamage during imaging. One-week-long storage was used to stabilize the cellular system and suppress the possibility of the short-term (several hours) cell degradation under the ambient conditions.

We performed spectroscopic measurements using a confocal Raman microscope (LabRAM HR Evolution, Horiba) with a 532 nm excitation laser using a laser beam focal spot size of ~ 1 μm . The optical microscope images of a typical RBC and R6G-stained RBC are shown in Fig. 1b and d, respectively. The typical RBC donut shape is seen in the optical image. The R6G-stained RBCs had a shallower donut shape due to the staining-induced echinocytosis, which is common in stained bovine blood smears.²³ The measured spectra of the RBC and R6G-stained RBC are shown in Fig. 1c and e, respectively. These spectra were obtained by integrating over the whole area of the cell with 1 s exposure time.

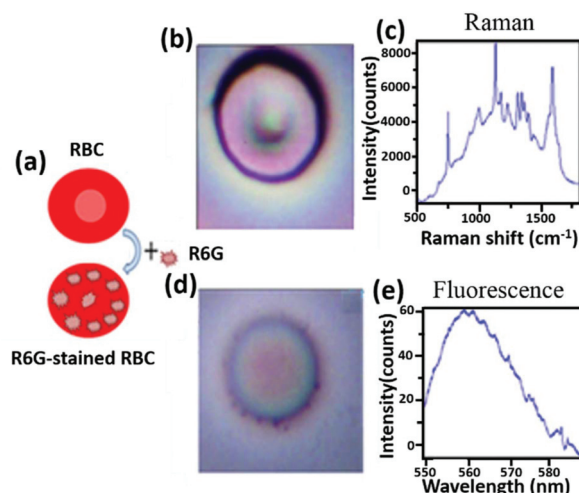


Fig. 1 (a) Schematic of the R6G-stained RBC preparation. Optical microscope images of RBC, 8×8 μm (b) and R6G-stained RBC, 10×10 μm (d) and the corresponding resonance Raman (c) and fluorescence (e) spectra. The spectrum of RBC is dominated by the resonance Raman signal of Hb, whereas the spectrum of R6G-stained RBC is dominated by the fluorescence of R6G (at low laser power).

3 Data processing algorithm

To separate the overlapping fluorescence and resonance Raman signals of R6G and RBC, we developed a data processing algorithm (using MATLAB (2015b)), which is included as a MATLAB script in the ESI.† An overview of the data processing algorithm is shown in Fig. 2. To reveal the Raman peaks, the raw spectrum data at each pixel was truncated to a region (approximately 20 cm^{-1} on either side of a peak) that encompasses the entirety of a single peak of interest (POI). An extra 10 cm^{-1} was included on each side in order to interpolate an accurate representation of any background around the POI such as that caused by neighboring peaks or broad background signals. Background removal was done after filtering. In fluorescence fitting, it was assumed that there is only a single fluorescence peak in the spectrum. Therefore, the raw spectrum data did not need to be truncated. If there were multiple fluorescence signals, the truncation function in the software could be used to isolate a single fluorescence peak.

The truncated spectral data was then filtered with a Savitzky–Golay filter to remove noise while maintaining spectral integrity. Savitzky–Golay filters use a linear least squares

polynomial fit of a chosen sized window and shift that window across the data set with the midpoint of each fit used as a new, filtered data point. Although a boxcar filter's averaging technique would help to remove the high frequency noise, it has a greater chance of leveling narrow peaks. Due to the polynomial nature of the Savitzky–Golay filter, the chance of leveling a peak is reduced²⁴ and, hence, Savitzky–Golay filters are used by most spectroscopic software packages.²⁵ Many combinations of filter orders and window sizes were considered before choosing a 4th order filter with a 21-point window as the best compromise between the noise reduction, spectral integrity, and spectral feature width. A 3×3 pixel, next-nearest-neighbor spatial filter was then run over the entire image to reduce white noise. This filter weighs each point on the cell with its 8 closest neighboring points in order to further reduce noise.

Again, multiple variations of the nearest-neighbor (weighted only with the 4 closest neighbors) and next-nearest-neighbor spatial filters were considered before choosing a next-nearest-neighbor filter. The center was weighted at 80% and the surrounding 8 pixels equally weighted at 2.5%, as the best method of reducing noise while still maintaining high frequency peaks in the spectrum.

In order to remove background from the Raman peaks caused by the neighboring Raman peaks and broader signals, a linear function was used to fit the background between the combined 20 cm^{-1} of extra points (10 cm^{-1} from both the beginning and end of the data set). This fit was then subtracted from the truncated data set to eliminate any background created by fluorescence or neighboring Raman peaks.

A fitting function was used to extract information about POI from the spectrum. The data was fit with either a Gaussian or a Lorentzian function and 4 parameters were measured and plotted in the spatial domain: normalized magnitude, center, width, and R^2 (Fig. 3).

The “normalized magnitude” plot in Fig. 3b shows where the vibrational signals corresponding to a particular chemical bond associated with the POI are concentrated. The “center” plot in Fig. 3c shows the location of the peak on the spectrum at each pixel. The “width” plot in Fig. 3d was used to check for the uniformity of the Raman peaks throughout the cell. The “ R^2 ” plot in Fig. 3e shows how well the Gaussian or Lorentzian functions fit the data. According to the R^2 values in this experiment, the Gaussian function was a cleaner fit to the Raman POI. The Raman peak fit at 1589 cm^{-1} is shown in Fig. 3. In order to eliminate fits that did not correspond to Raman peaks, the width and R^2 values were checked at each pixel to ensure a narrow, well fit Raman peak. If either the value of R^2 was less than 0.2 or the width value was outside of the truncated boundaries, all four parameters at that pixel were set to zero. When looking for a fluorescence peak, the fluorescence signal is much wider than any individual Raman peak and therefore, the impact of the Raman signal on the fluorescence fit is negligible. Also, since the entirety of the fluorescence signal is not always collected in the range of this spectrum, subtracting the background has a chance of skewing the

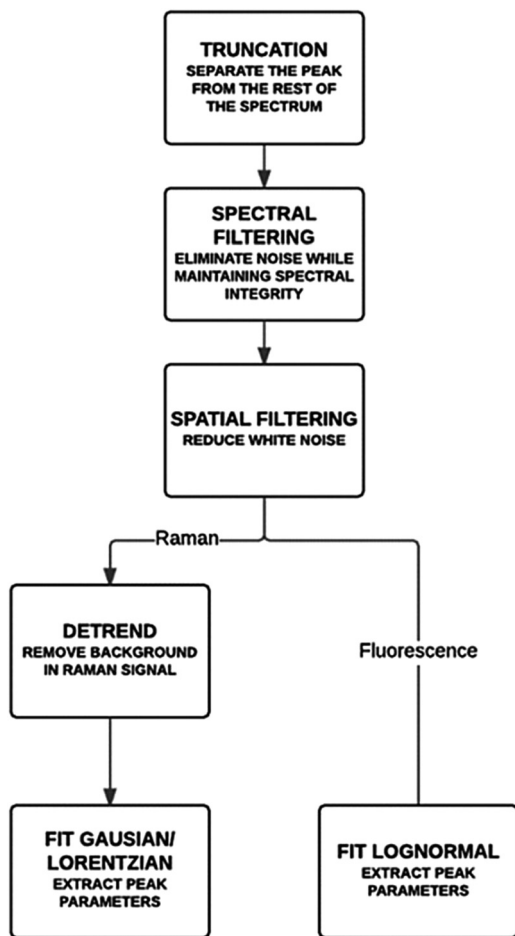


Fig. 2 Overview of the data processing algorithm for separating and analyzing the fluorescence and resonance Raman spectra.

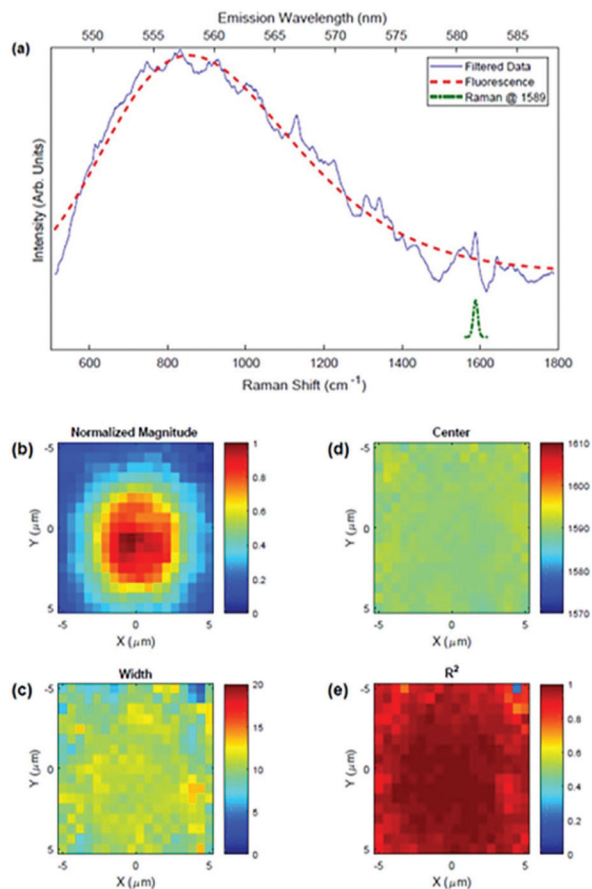


Fig. 3 (a) Filtered mixed Raman scattering and fluorescence signal (blue) from an R6G-stained RBC (exposed to 532 nm laser at 0.2 mW for 0.1 s) with overlaid fitting curves of fluorescence at 555 nm (dashed red) and Raman scattering signal at 1589 cm^{-1} (dash-dotted green). (b)–(e) The corresponding examples of the data processing software output.

results. Therefore, no background was subtracted before fitting the data to the lognormal function,

$$\varepsilon(\tilde{\nu}) = \frac{\varepsilon_0 b}{\tilde{\nu} - a} \exp(-c^2) \exp\left\{-\frac{1}{2c^2} \left[\ln\left(\frac{\tilde{\nu} - a}{b}\right)\right]^2\right\}; \quad \tilde{\nu} > a, \quad (1)$$

Where a , b , and c are the parameters related to the position of the mode, ν_0 (cm^{-1}), the half-width, H (cm^{-1}), and the empirical measure of the skewness, ρ by the equations

$$c = \frac{\ln \rho}{\sqrt{2 \ln 2}}, \quad (2)$$

$$b = H \frac{\rho}{\rho^2 - 1} \exp(c^2), \quad (3)$$

$$a = \tilde{\nu}_0 - H \frac{\rho}{\rho^2 - 1}. \quad (4)$$

Siano *et al.*, among others, observed that a lognormal function is a better fit for the fluorescence spectrum than a Gaussian function due to its ability to mimic the Gaussian while also allowing for asymmetric shapes.²⁶ They were also able to use the function in eqn (1) to separate multiple fluo-

rescent signals from one another when found in the same spectrum. Similar to the Raman image plots, the fluorescence image plots are composed of four subplots: normalized fluorescence intensity, asymmetry, width, and R^2 . If there is no fluorescence signal in the spectrum, an offset in magnitude of the filtered data would be likely where there is a significant contribution of the Raman signal. This is likely to occur because the background is not removed from the fluorescence data causing the “normalized fluorescence” plot to show a clear image of the cell even though the R^2 values are near zero. Therefore, if the R^2 value was less than 0.2, all the parameters associated with the pixel were set to zero. This reduces the chances of a false positive identification of fluorescence in a spectrum. The “asymmetry” and “width” plots were both used to check uniformity across the cell. The R^2 plot was used to identify how well the lognormal curve fitted the data. A typical fluorescence peak fit is shown in Fig. 3a.

The filtered data from the fluorescence processing is also used to identify the pixels from which a spatially averaged spectrum for each cell is generated (Fig. 4m–r). The Raman and fluorescence images were used to identify where the cell boundaries lie in terms of the pixels. Then, a rectangular area of the pixels that reside entirely within the cell were summed and averaged in order to create a spectrum plot that is representative of the cell as a whole.

4 Results and discussion

To investigate the effects of the laser power on imaging and photodamage, we selected 1-week old cells to suppress the effects of early aging during the imaging process. Due to the relative weakness of the Raman signals, the complete acquisition of all the spectroscopic images for one cell using different laser powers takes up to several hours. Therefore, it is desirable to select a cell, which has already been aged for several days to eliminate the effects of early aging. To evaluate the photostability of the stained cells we performed spectroscopic measurements on 1-week old R6G-stained RBCs using 532 nm laser excitation. Fig. 4 shows the fluorescence and resonance Raman spectra and images obtained with 1 s accumulation time at 0.2 μW , 2 μW , 20 μW , 75 μW , 0.2 mW, and 0.3 mW laser powers, focused on the sample. The spectra were integrated over the whole cell and show a large contribution of the R6G fluorescence at low laser powers and a gradual transition into the bleached spectra with the large contributions of Hb and R6G Raman signals at high powers. The corresponding extracted fluorescence (555 nm) and Raman (1590 cm^{-1} band) images reveal the anti-correlated spatial dependence of the two signals for different laser powers.

The 75 μW laser power with 1 s accumulation time provides the optimal compromise of the signal-to-noise (SNR) ratios of the two signals. This allows acquisition of the highest quality images for the fluorescence and Raman signals simultaneously. Therefore, we have chosen a fresh RBC cell at 75 μW laser power as the control for the data analysis throughout this paper.

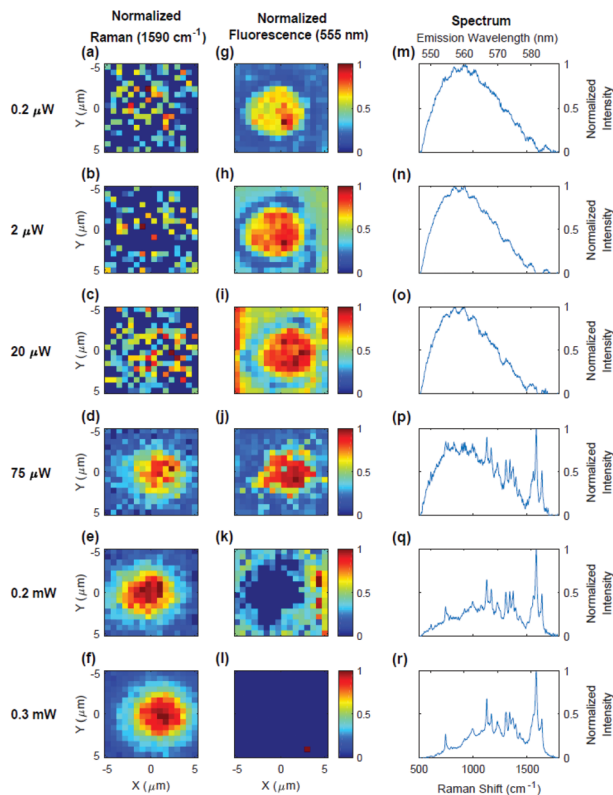


Fig. 4 Resonance Raman (a)–(f) and fluorescence (g)–(l) images and the corresponding spectra (m)–(r) of the 1-week old R6G-stained RBC. The images were obtained by integrating the spectral intensity of the 1590 cm^{-1} Raman band of Hb in (a)–(f) and of the 555 nm fluorescence band of R6G in (g)–(l). The spectra and images show the gradual transition between the fluorescence and Raman signals as a function of the laser power that was varied from 0.2 μW to 0.3 mW at the sample.

The spectrum and images at 75 μW laser power show clear signatures of the broad R6G fluorescence band and narrow Raman peaks of Hb (Fig. 4d, j and p). For higher laser powers, the fluorescence signal of R6G is suppressed (Fig. 4q and r) and the Raman signals dominate. We performed the spectral analysis and band assignment based on the previous work on RBC^{27–30} and R6G.³¹ We identified Raman bands, which correspond to 17 vibrational transitions. Table 1 shows the measured Raman shifts and band assignments for the Raman spectra of the unstained dried fresh RBC at 75 μW laser power (control), and dried fresh and 1-week old R6G-stained RBC for different laser powers.

These Raman shifts were obtained by the fitting procedure described above. Table 1 shows that the Raman shifts fluctuate within several cm^{-1} . However, the relative separation of the corresponding different vibrational transitions is on the order of tens of cm^{-1} that makes them clearly distinguishable.

Fig. 5 shows a comparison of the Raman spectra of the unstained dried fresh RBC (control) with the dried fresh R6G-stained RBC at 75 μW laser power. All spectral band intensities were normalized to the maximum of the 1590 cm^{-1} band, which was the highest intensity band observed in all the spectra in this work. The signals of the R6G-stained RBC show strong bands at 770 cm^{-1} (peak 3) and 1645 cm^{-1} (peak 17), which are attributed to R6G. The ratios of the other bands in the 1500–1650 cm^{-1} spectral range do not significantly change, indicating the stability of the dried fresh RBC upon staining.²⁷

Fig. 6 presents the Raman spectral analysis of aging effects of the R6G-stained RBC samples at 0.3 mW excitation. All spectral band intensities were normalized to the maximum intensity of the 1590 cm^{-1} band. No significant changes were observed in the Raman spectra of the 1-week old R6G-stained

Table 1 Raman shifts (in cm^{-1}) and band assignments of the unstained dried fresh RBC at 75 μW laser power (control), dried fresh, and 1-week old R6G-stained RBC for different laser powers

Peak no.	Unstained dried fresh RBC at 75 μW (control)	R6G-stained dried fresh RBC at 75 μW	R6G-stained dried fresh RBC at 0.3 mW	R6G-stained 1-week old RBC at 75 μW	R6G-stained 1-week old RBC at 0.3 mW	R6G-stained 1-week old RBC at 0.9 mW	RBC band assignment	R6G band assignment
1	748	749	749	747	747	747	ν_{15}, γ_1	—
2	760	764	762	760	760	759	ν_{15}, γ_1	—
3	768	768	774	771	773	771	—	C–H op bend
4	1129	1131	1132	1129	1128	1129	ν_5	C–H ip bend
5	1144	1148	1146	1145	1146	1146	ν_{14}	—
6	1156	1165	1156	1154	1157	1165	ν_{44}	—
7	1173	1173	1172	1170	1171	1172	ν_{30}	—
8	1307	1312	1311	1308	1307	1308	ν_{21}	Aromatic C–C str
9	1339	1346	1344	1343	1340	1341	ν_{41}^d	—
10	1360	1368	1364	1360	1360	1360	ν_4	Aromatic C–C str
11	1374	1380	1376	1373	1374	1372	ν_4	—
12	1395	1401	1399	1397	1395	1396	ν_{20}	—
13	1544	1547	1549	1546	1544	1545	ν_{11}	—
14	1559	1565	1564	1563	1561	1560	ν_2	—
15	1587	1590	1589	1587	1586	1586	ν_{37}	—
16	1625	1625	1625	1625	1625	1625	$\nu_{10}, \nu(\text{C}=\text{C})$	—
17	1641	1641	1643	1640	1640	1640	—	Aromatic C–C str

Abbreviations: ν , ip: in plane mode, γ , op: out of plane mode, str: stretching.

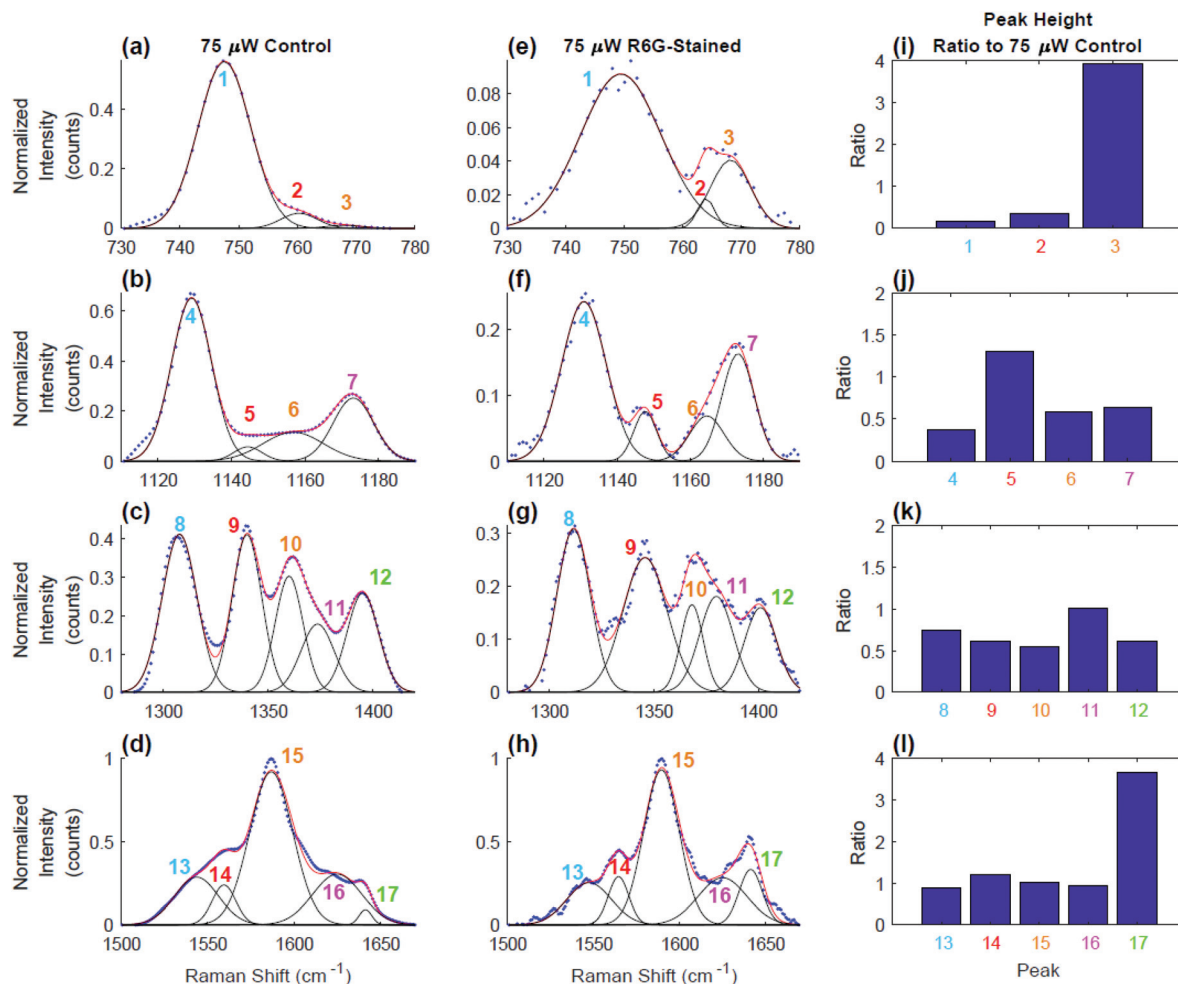


Fig. 5 Raman spectra of the dried fresh unstained control RBC (a–d) and dried fresh R6G-stained RBC (e–h) normalized to the intensity of the 1590 cm^{-1} band at $75\text{ }\mu\text{W}$ laser power show the absence of the significant staining effects on RBC. The observed strong intensities of bands 3 and 17 are attributed to the resonance Raman signals of R6G. Solid black lines are the Gaussian fits of the selected marked bands and solid red lines are the combined fits. (i–l) Peak height ratios of the normalized peak intensities of the dried fresh R6G-stained RBC to the normalized peak intensities of the unstained dried fresh RBC (control) at $75\text{ }\mu\text{W}$.

RBC compared to the dried fresh R6G-stained RBC in the $1500\text{--}1650\text{ cm}^{-1}$ spectral range, except a small reduction of the intensity of the R6G band 17. However, the changes in the relative ratios of the bands in the other three spectral ranges, namely, the $730\text{--}780\text{ cm}^{-1}$ (6a, 6e), $1120\text{--}1180\text{ cm}^{-1}$ (6b, 6f), and $1300\text{--}1400\text{ cm}^{-1}$ (6c, 6g) ranges relative to the 1590 cm^{-1} band were observed (6i–6k).

Fig. 7 shows the Raman spectra of the 1-week old R6G-stained RBC obtained at $75\text{ }\mu\text{W}$ (a–d) and 0.9 mW (e–h) laser powers. All spectral band intensities were normalized to the maximum intensity of the 1590 cm^{-1} band. The spectra show dramatic changes of the relative Raman band intensities of the R6G bands 3 (at 770 cm^{-1}) and 17 (1645 cm^{-1}) relative to the band of RBC at 1590 cm^{-1} .

With the increase of laser power from $75\text{ }\mu\text{W}$ to 0.9 mW , there is a drastic decrease of the normalized Raman intensity in the R6G bands 3 and 17, which may be attributed to the photobleaching of the R6G fluorescence and resonance

Raman signals. The relative ratios of the other RBC bands do not change much with laser power, which reveals the photostability of the R6G-stained RBC upon the bleaching of the R6G signals.

When comparing the Raman signals between the stained and unstained cells (Fig. 5), dried fresh and aged cells (Fig. 6), and among the different laser powers (Fig. 7), care has to be taken for the quantitative analysis of the peak height ratios. For example, the overall shapes of the Raman spectra of the stained and the unstained RBCs in Fig. 5 are similar with the exception of peaks 3 and 17, which are attributed almost exclusively to R6G. The four strong Raman peaks (13–16 in the $1500\text{ cm}^{-1}\text{--}1650\text{ cm}^{-1}$ spectral range) do not show any significant changes with a peak ratio of ~ 1 . However, the peak height ratios of the other peaks in the $1120\text{ cm}^{-1}\text{--}1180\text{ cm}^{-1}$ and $1300\text{ cm}^{-1}\text{--}1400\text{ cm}^{-1}$ ranges are approximately two times smaller. The peak height ratios are even smaller in the $730\text{ cm}^{-1}\text{--}780\text{ cm}^{-1}$ range. We attribute these peak height ratio

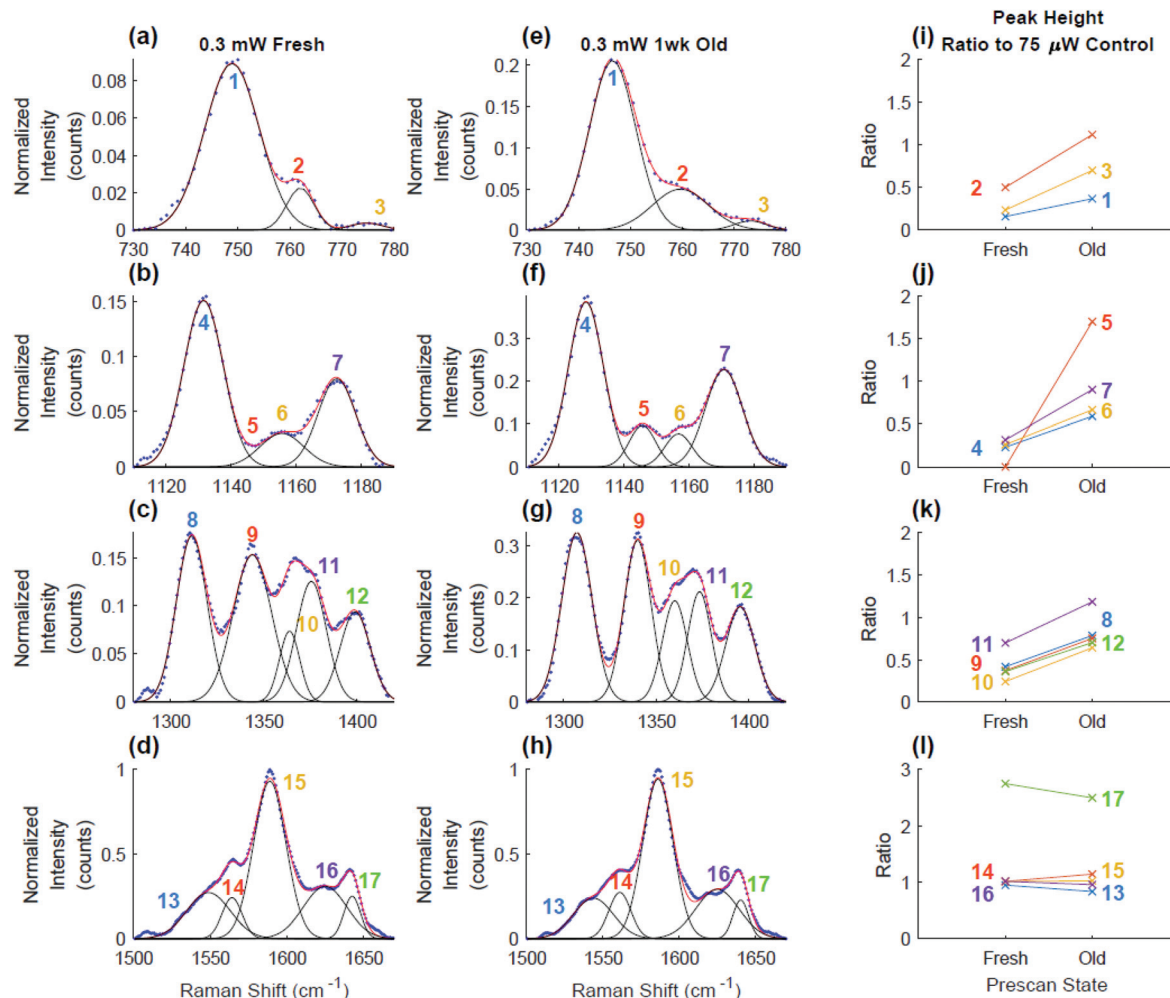


Fig. 6 Raman spectra of the dried fresh (a–d) and the 1-week old (e–h) R6G-stained RBC at 0.3 mW laser power normalized to the intensity of the 1590 cm⁻¹ band show the absence of the significant differences due to aging of the stained RBCs. Solid black lines are the Gaussian fits to the selected marked bands and solid red lines are the combined fits. (i–l) Peak height ratios of the normalized peak intensities of the dried fresh and 1-week old R6G-stained RBCs at 0.3 mW laser power to the corresponding normalized peak intensities of the unstained dried fresh RBC (control) at 75 μW.

variations to the decrease of the SNR of the Raman signals deconvoluted from the large fluorescence background. Indeed, the overlap between the Raman and fluorescence signals is strongest for the 730 cm⁻¹–780 cm⁻¹ range and weakest for the 1500 cm⁻¹–1650 cm⁻¹ spectral range, as can be seen in Fig. 3a. Therefore, we conclude that the peak height ratios provide the most useful information by the comparison of the peaks which are not far from each other in the same spectral range. The quantitative comparison of the peaks located in different spectral ranges is limited and should be performed with care when a large contribution of the fluorescence background is present. Similar effects are observed by comparing Raman spectra of the dried fresh and 1-week old R6G-stained RBCs in Fig. 6. The overall spectral shapes in all the ranges are similar except peak 1 in the 730 cm⁻¹–780 cm⁻¹ range, which gets stronger in the 1-week old cell. All peaks in the 1500 cm⁻¹–1650 cm⁻¹ range maintain their peak ratio, except peak 17 which decreases a little, probably due to a slow desorption of R6G during aging.

Contrary to the results in Fig. 5, most of the peaks in the 1120 cm⁻¹–1180 cm⁻¹ and 1300 cm⁻¹–1400 cm⁻¹ ranges in Fig. 6 become approximately two times stronger but do not change their relative peak ratios. This agrees with the interpretation of the partial masking of the Raman signals by the fluorescence background from R6G. During the cell aging, R6G partially desorbs, reducing the amount of fluorescence and, therefore, leads to the increase in the measured Raman signals of RBC.

In summary, we performed simultaneous spectroscopic bio-imaging and photostability analysis of R6G stained RBCs using fluorescence and resonance Raman scattering of 532 nm laser excitation. We developed a data processing algorithm for separating these signals and as a result, observed no significant photodamage of RBC under the complete photobleaching of R6G. We explored excitation laser power dependence and identified spectral ranges which provide reliable spectroscopic signatures of RBC photodamage and R6G bleaching. Our general approach may be used to investigate the photostability

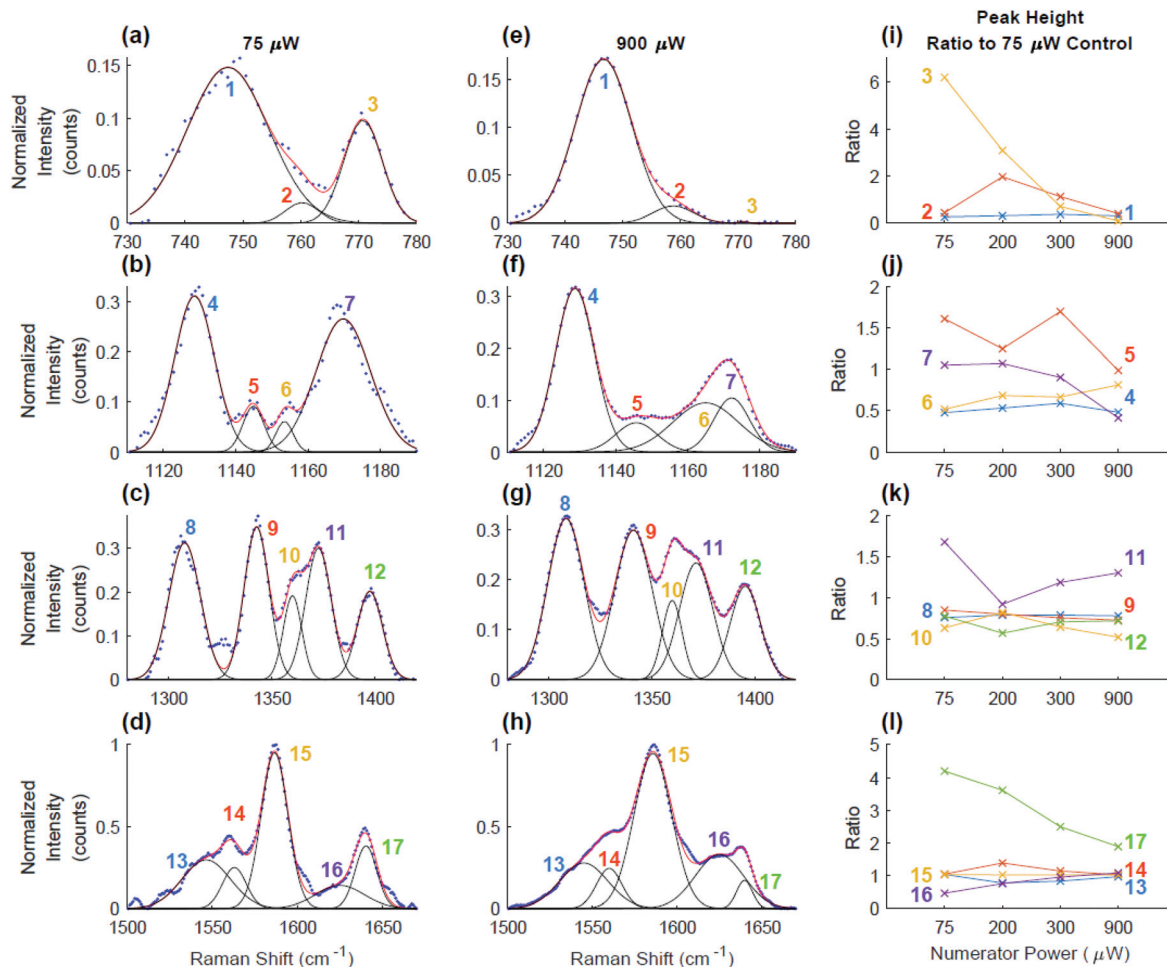


Fig. 7 Raman spectra of the 1-week old R6G-stained RBC at 75 μW (a)–(d) and at 0.9 mW (e)–(h) laser powers normalized to the intensity of the 1590 cm^{-1} band show the absence of the significant laser power effects on the Hb signals of RBC and the significant spectral differences of the bands 3 and 17 due to the bleaching of R6G. Solid black lines are the Gaussian fits of the selected marked bands and solid red lines are the combined fits. (i–l) Peak height ratios of the normalized peak intensities of the 1-week old R6G-stained RBC at different laser powers to the normalized peak intensities of the unstained dried fresh RBC (control) at 75 μW .

of different staining molecules by matching the corresponding excitation laser frequency and applied to more complex systems such as leukocytes, cancer, and other types of cells. Additionally, our approach can be extended to coherent Raman spectroscopy, such as coherent anti-Stokes Raman scattering (CARS), which will allow for the fast imaging of cells in a few seconds time. Effects of ultrashort laser pulses used in CARS may also be investigated. Finally, our approach may also be used to investigate photostability effects in cells and biomolecules using surface-enhanced Raman scattering (SERS) and surface-enhanced fluorescence (SEF) spectroscopies as well as their interplay, as these techniques are based on strong electric fields generated by the plasmonic nanoparticles.

Conflicts of interest

The authors declare that there are no conflicts of interest related to this article.

Acknowledgements

We acknowledge the support of the National Science Foundation (Grant No. CHE-1609608), the Air Force Office of Scientific Research (Award No. FA9550-18-1-0141), the Office of Naval Research (Grant No. N00014-16-1-2578), the Robert A. Welch Foundation (Awards A-1261 and A-1547), and the National Institutes of Health (1R21DK091862-01A1).

References

- 1 S. H. Yun and S. J. J. Kwok, Light in Diagnosis, Therapy and Surgery, *Nat. Biomed. Eng.*, 2017, **1**, 0008.
- 2 K. Ramser, Raman spectroscopy of single cells for biomedical applications, *Adv. Biomed. Spectrosc.*, 2012, **5**, 106–147.
- 3 C. Balas, Review of biomedical optical imaging—a powerful, non-invasive, non-ionizing technology for

- improving in vivo diagnosis, *Meas. Sci. Technol.*, 2009, **20**(10), 104020.
- 4 R. Smith, K. L. Wright and L. Ashton, Raman spectroscopy: an evolving technique for live cell studies, *Analyst*, 2016, **141**(12), 3590–3600.
 - 5 A. Germond, V. Kumar, T. Ichimura, J. Moreau, C. Furusawa, H. Fujita, *et al.*, Raman spectroscopy as a tool for ecology and evolution, *J. R. Soc., Interface*, 2017, **14**(131), 20170174.
 - 6 B. R. Wood, P. R. Stoddart and D. McNaughton, Molecular imaging of red blood cells by Raman spectroscopy, *Aust. J. Chem.*, 2011, **64**(5), 593–599.
 - 7 N. K. Das, Y. Dai, P. Liu, C. Hu, L. Tong, X. Chen, *et al.*, Raman Plus X: Biomedical Applications of Multimodal Raman Spectroscopy, *Sensors*, 2017, **17**(7), 1592.
 - 8 S. Saurabh, A. M. Perez, C. J. Comerci, L. Shapiro and W. Moerner, Super-resolution imaging of live bacteria cells using a genetically directed, highly photostable fluoromodule, *J. Am. Chem. Soc.*, 2016, **138**(33), 10398–10401.
 - 9 A. von Diezmann, Y. Shechtman and W. Moerner, Three-Dimensional Localization of Single Molecules for Super-Resolution Imaging and Single-Particle Tracking, *Chem. Rev.*, 2017, **117**(11), 7244–7275.
 - 10 J. H. WANG, J. Bartlett, A. Dunn, S. Small, S. Willis, M. Driver, *et al.*, The use of rhodamine 6G and fluorescence microscopy in the evaluation of phospholipid-based polymeric biomaterials, *J. Microsc.*, 2005, **217**(3), 216–224.
 - 11 M. W. Berns, A. E. Siemens and R. J. Walter, Mitochondrial fluorescence patterns in rhodamine 6G-stained myocardial cells in vitro, *Cell Biophys.*, 1984, **6**(4), 263–277.
 - 12 X. N. He, Y. Gao, M. Mahjouri-Samani, P. N. Black, J. Allen, M. Mitchell, *et al.*, Surface-enhanced Raman spectroscopy using gold-coated horizontally aligned carbon nanotubes, *Nanotechnology*, 2012, **23**(20), 205702.
 - 13 P. Li, X. Zhou, H. Liu, L. Yang and J. Liu, Surface-enhanced Raman evidence for Rhodamine 6G and its derivative with different adsorption geometry to colloidal silver nanoparticle, *J. Raman Spectrosc.*, 2013, **44**(7), 999–1003.
 - 14 A.-I. Henry, B. Sharma, M. F. Cardinal, D. Kourouski and R. P. Van Duyne, Surface-enhanced Raman spectroscopy biosensing: In vivo diagnostics and multimodal imaging, *Anal. Chem.*, 2016, **88**(13), 6638–6647.
 - 15 K. A. Willets, S. M. Stranahan and M. L. Weber, Shedding light on surface-enhanced Raman scattering hot spots through single-molecule super-resolution imaging, *J. Phys. Chem. Lett.*, 2012, **3**(10), 1286–1294.
 - 16 J. Fölling, M. Bossi, H. Bock, R. Medda, C. A. Wurm, B. Hein, *et al.*, Fluorescence nanoscopy by ground-state depletion and single-molecule return, *Nat. Methods*, 2008, **5**(11), 943–945.
 - 17 T. Egawa and S.-R. Yeh, Structural and functional properties of hemoglobins from unicellular organisms as revealed by resonance Raman spectroscopy, *J. Inorg. Biochem.*, 2005, **99**(1), 72–96.
 - 18 D. Rousseau and M. Ondrias, Resonance Raman scattering studies of the quaternary structure transition in hemoglobin, *Annu. Rev. Biophys. Bioeng.*, 1983, **12**(1), 357–380.
 - 19 S. Hoey, D. Brown, A. McConnell, W. Smith, M. Marabani and R. Sturrock, Resonance Raman spectroscopy of hemoglobin in intact cells: a probe of oxygen uptake by erythrocytes in rheumatoid arthritis, *J. Inorg. Biochem.*, 1988, **34**(3), 189–199.
 - 20 B. R. Wood, P. Caspers, G. J. Puppels, S. Pandiancherri and D. McNaughton, Resonance Raman spectroscopy of red blood cells using near-infrared laser excitation, *Anal. Bioanal. Chem.*, 2007, **387**(5), 1691–1703.
 - 21 R. D. Snook, T. J. Harvey, E. C. Faria and P. Gardner, Raman tweezers and their application to the study of singly trapped eukaryotic cells, *Integr. Biol.*, 2009, **1**(1), 43–52.
 - 22 C. Eggeling, A. Volkmer and C. A. Seidel, Molecular photobleaching kinetics of Rhodamine 6G by one- and two-photon induced confocal fluorescence microscopy, *ChemPhysChem*, 2005, **6**(5), 791–804.
 - 23 N. C. Jain, *Essentials of Veterinary Hematology*, Lea & Febiger, Philadelphia, 1993.
 - 24 A. Savitzky and M. J. Golay, Smoothing and differentiation of data by simplified least squares procedures, *Anal. Chem.*, 1964, **36**(8), 1627–1639.
 - 25 M. Člupěk, P. Matejka and K. Volka, Noise reduction in Raman spectra: Finite impulse response filtration versus Savitzky-Golay smoothing, *J. Raman Spectrosc.*, 2007, **38**, 1174–1179.
 - 26 D. B. Siano and D. E. Metzler, Band Shapes of the Electronic Spectra of Complex Molecules, *J. Chem. Phys.*, 1969, **51**, 1856–1861.
 - 27 B. R. Wood and D. McNaughton, Raman excitation wavelength investigation of single red blood cells in vivo, *J. Raman Spectrosc.*, 2002, **33**, 517–523.
 - 28 A. Bankapur, E. Zachariah, S. Chidangil, M. Valiathan and D. Mathur, Raman tweezers spectroscopy of live, single red and white blood cells, *PLoS One*, 2010, **5**(4), e10427.
 - 29 G. Rusciano, A. C. De Luca, G. Pesce and A. Sasso, Raman Tweezers as a Diagnostic Tool of Hemoglobin-Related Blood Disorders, *Sensors*, 2008, **8**(12), 7818–7832.
 - 30 M. A. Khiavi, A. Mechler, K. R. Bamberg, D. McNaughton and B. R. Wood, A resonance Raman spectroscopic investigation into the effects of fixation and dehydration on heme environment of hemoglobin, *J. Raman Spectrosc.*, 2009, **40**, 1668.
 - 31 M. Wahadoszamen, A. Rahaman, N. M. R. Hoque, A. I. Talukder, K. M. Abedin and A. F. M. Y. Haider, Laser Raman Spectroscopy with Different Excitation Sources and Extension to Surface Enhanced Raman Spectroscopy, *J. Spectrosc.*, 2015, **2015**, 1–8.